



Optimization of stationary shoulder friction stir welding numerical model based on instantaneous velocity center

Wang Jiang¹ · Chaojiang Li¹ · Tao Yuan² · Shujun Chen² · Hao Jing¹

Received: 24 March 2023 / Accepted: 6 September 2023 / Published online: 18 September 2023
© The Author(s), under exclusive licence to Springer-Verlag London Ltd., part of Springer Nature 2023

Abstract

During the friction stir welding process, the motion of the stirring tool is divided into two parts: the rotational motion and the lateral feed, both of which influence the temperature distribution, material flow, and slip rate. The effect of the rotational motion in numerical simulations is usually the focus of research, but the changes in material flow, slip, and heat generation due to welding speed are usually neglected. In this study, the numerical model of stationary shoulder friction stir welding (SSFSW) was developed to optimize the effect of welding speed on heat generation and material flow based on the instantaneous velocity center (IVC), and the relationship between n/v and IVC were discussed. The instantaneous velocity center distance was inversely proportional to n/v , and its magnitude affected the difference in temperature between the AS and RS.

Keywords Instantaneous velocity center · Heat production · Material flow · Slip rate

1 Introduction

Friction stir welding (FSW) has been widely studied all over the world since it was invented in the year 1991 [1]. However, a large amount of heat is generated on the weld surface using rotating shoulder in FSW, which leads to a significant temperature gradient along the thickness direction of the weld. Generally, larger temperature gradients show a degradation of various mechanical and corrosion properties.

Therefore, suppressing the rotation of the shoulder and thus producing a smaller temperature gradient becomes crucial to improving the performance of the FSW weld. In contrast to the conventional FSW, stationary shoulder friction stir welding (SSFSW) employs a rotating stirring pin and a stationary shoulder, resulting in reduced temperature gradients within the weld.

Stationary shoulder friction stir welding (SSFSW) has been widely used in joining many structural engineering materials, such as aluminum alloys and titanium alloys [2, 3]. The process parameters of the SSFSW determined the temperature distribution, material flow, phase transformation, and recrystallization processes during the welding process, which affects the mechanical properties of the weld to some extent. The optimization of the SSFSW process, therefore, requires quantification of the temperature distribution and material flow during the welding process [4–6]. The conventional experimental methods are not easy to investigate the temperature and material flow patterns during the welding process because SSFSW involves highly coupled thermomechanical processes [7–9]. Numerical simulation based on computational fluid dynamics (CFD) has a greater advantage in studying these phenomena. However, the reliability of the numerical simulation depends on many aspects, such as heat generation models and boundary conditions [10, 11].

In the numerical simulation of SSFSW, the boundary conditions between the stirring tool and welded materials

✉ Tao Yuan
ty29@bjut.edu.cn

Wang Jiang
jiangwang199602@163.com

Chaojiang Li
cjli85@126.com

Shujun Chen
sjchen@bjut.edu.cn

Hao Jing
jinghao1998@foxmail.com

¹ School of Mechanical Engineering, Beijing Institute of Technology, 5 South Zhongguancun Street, Haidian District, Beijing 100081, China

² Faculty of Materials and Manufacturing, Institute of Intelligent Forming Equipment and System, Beijing University of Technology, Beijing 100124, People's Republic of China

have been extensively investigated by many scholars [12, 13]. And the boundary conditions are limited by many factors such as temperature, speed, pressure, deformation, and the geometry of the mixing tool. Due to the complexity of the welding process, the boundary conditions are mainly divided into two main kinds: boundary velocity (BV) models and boundary shear stress conditions (BSS) models. Boundary velocity models applied at the contact interface between the workpiece, and the stirring tool was shown by function of slip, temperature, and rotation speed. A vector velocity at the tool/workpiece interface was applied in the velocity boundary model. The most commonly used BV model is the “sticking” model, which assumes that there will be no sliding at the interface between the welding tool and the workpiece. However, some researchers have found that the contact state at the tool/workpiece interface is neither a pure sliding state nor an adhesive state. Therefore, they introduced the δ parameter in the heat generation model, which can represent different contact states at the interface. Shi et al. [14] proposed a novel model of the FSW to predict weld formation based on the BV model. The results demonstrate that, under optimized welding conditions, the plastic material flows in the horizontal direction and concomitantly fills the entirety of the cavity located at the rear of the tool, thereby forming a structurally sound weld. Wu et al. [15–17] developed a numerical model based on BV model to investigate the coupled acoustic action-heat generation-plastic deformation behaviors in ultrasonic-assisted FSW systems. The results show that the ultrasound induces a notable increment in the proportion of viscous dissipation heat within the overall heat generation processes. The heat transfer and visco-plastic flow of Ti-6Al-4V during FSW had been investigated by Nandan et al. [18–20]. The computed results show that the interface between the tool and workpiece predominantly exhibited a condition of near-sticking. Liu et al. [21] performed numerical simulations of spatial heat transfer and 3D visco-plastic flow in vortex-FSW using a CFD analysis. A fluid–solid-interaction algorithm was established for the coupling model by Huang et al. [22] using a combination of numerical modeling of plastic flow and experiments to investigate the mechanism of joint formation.

In the numerical simulation of FSW, the BSS model is used as an alternative form of the BV model. The most important consideration in boundary conditions is to determine the contact state, the sliding/adhesion state. The automatic conversion was achieved in the BSS boundary condition between contact states by considering the static friction effect, which is of great significance for predicting the sliding and adhesion states at the tool/workpiece interface. The BSS boundary condition was incorporated by Liechty et al. [23] in the computational fluid dynamics (CFD) modeling of FSW. The BSS boundary condition is the application of shear stress at the contact interface, which permits areas of significant slip, while shear stresses

at other regions approach the flow stress of the material. A numerical simulation was conducted by Chen et al. [24–26] to analyze the heat transfer, plastic deformation behaviors, and viscous slip transitions in interfaces at the BSS conditions during the FSW. An analytical model based on BSS was established by Wang et al. [27] to correlate the stick-slip fraction to derive dimensionless functions for torque and heat-generation rate predictions.

Although many studies have been published, the slip caused by the welding speed during the welding process, which leads to changes in heat production and boundary conditions, has usually been ignored [28]. In the previous study [29, 30], the ratio of welding speed to the rotation speed was fitted and presented the instantaneous velocity center (IVC) of the stirring tool but did not discuss further the effect of the IVC on the numerical model. If the numerical model of SSFSW can be optimized based on IVC and the effect of welding speed on heat production and slip can be corrected, the motion pattern during the welding process can be understood much more clearly.

Therefore, this study established the three-dimensional numerical models of the SSFSW, focusing on the effect of the instantaneous velocity center on the welding process. The heat generation, material flow, and slip rate during welding between the BV model and BSS model based on the IVC were compared. In addition, the relationship between n/v and the instantaneous velocity center of pin was discussed.

2 Experimental procedure

In this study, the Ti6AL4V titanium alloy is used for the workpiece material, and its chemical composition is 6.51% Al, 0.18% Fe, 4.13% V, 0.158% O, 0.02% C, 0.01% N (all wt.%) and Ti(Bal). The size of the plates was 300 mm long, 150 mm wide, and 3.2 mm thick. The welding speed is 15 mm/min, and the rotation speed of pin is 500/400/300 rpm. The diameter of stationary shoulder was 12 mm, and the diameter of the top and the bottom of pin without thread was 8 mm and 5 mm, respectively. During the welding process, the stationary shoulder is in contact with the substrate but does not rotate; it is fed laterally with the stirring tool. A plunge depth of 0.1 mm was employed, and no tilt angle was adopted in the welding process.

3 Numerical modeling

Figure 1 shows the numerical simulation model. The geometric dimension of the workpiece of the model was considered the same as those used in the experiment. In the numerical model, both BV and BSS models were performed to apply rotational velocity to the stirring tool based on the instantaneous velocity center. Figure 1 shows the numerical

simulation of the welding parameters and three-dimensional Cartesian coordinate system, where the welding direction for the positive direction of the x -axis; z -axis is perpendicular to the surface of the workpiece; the origin is located at the bottom of the workpiece, using Gambit to discretize the grid before the calculation; the mesh size around the stirring tool is about 0.01 mm.

3.1 Heat generation

Friction and plastic deformation heats were synchronously considered. The heat input from plastic deformation is a volumetric heat flux, as given by [18]:

$$S_v = \beta_1 \times \sigma \times \dot{\epsilon} \tag{1}$$

where β_1 is the conversion efficiency of mechanical energy into heat in the shear layer of the workpiece and heat generation efficiency, σ is the flow stress and $\dot{\epsilon}$ is the plastic strain rate.

The heat generated by friction during the welding process was considered to be the surface heat flux at the tool/workpiece interface, which was determined by the shear stress and the relative velocity between the tool and the workpiece. In previous studies [29, 30], we had a projection of the welding speed in the direction of the shear stress, and the effect of the slip generated by the welding speed on heat production was ignored. This results in neglecting the effect of slip generated by welding speed on heat generation, and there may also be some error in the projected pinch angle. Therefore, our correction for the heat source model was based on the instantaneous velocity center, which can both reflect the slip of the welding speed in the heat production and correct for errors in the projection angle of the welding speed, as shown in Fig. 2.

3.1.1 Heat source model of boundary velocity

The speed at any point on the stirring tool is given as follows:

$$v_c = \omega r_c \tag{2}$$

where r_c is the distance from any point on the stirring tool to the instantaneous velocity center, v_c is the distance from any point on the stirring tool to the instantaneous velocity center multiplied by the angular velocity ω . At the interface, the contact shear stress is always parallel to the tangential direction of the interface.

If the velocity v_c of the pin at a point parallel to the tangential direction of the interface, the formula for heat generation by friction can be given by [31] the following:

$$q(r) = \beta_2 \times \tau_0 \times v_c \tag{3}$$

$$\beta_2 = \frac{\sqrt{(k\rho c_p)_D}}{\sqrt{(k\rho c_p)_D} + \sqrt{(k\rho c_p)_T}} \tag{4}$$

where β_2 is the heat production coefficient; $k, \rho,$ and c_p are the thermal conductivity, density, and heat capacity, respectively [32, 33]. The subscripts “D” and “T” respectively represent the workpiece and tool, where τ_0 is the frictional shear stress; v_c is the welding speed; however, if the direction of the velocity v_c of the stirring tool is at an angle to the tangential direction of the interface, then the formula of heat production by friction can be written as [34] follows:

$$q = \beta_2 \times \tau_0 \times v_c \cos(\beta - \theta) \tag{5}$$

After the above analysis, the expressions for the heat flux at the shoulder, the pin side and the bottom of the stirring tool during SSFSW welding are given in Eqs. (6–8), respectively:

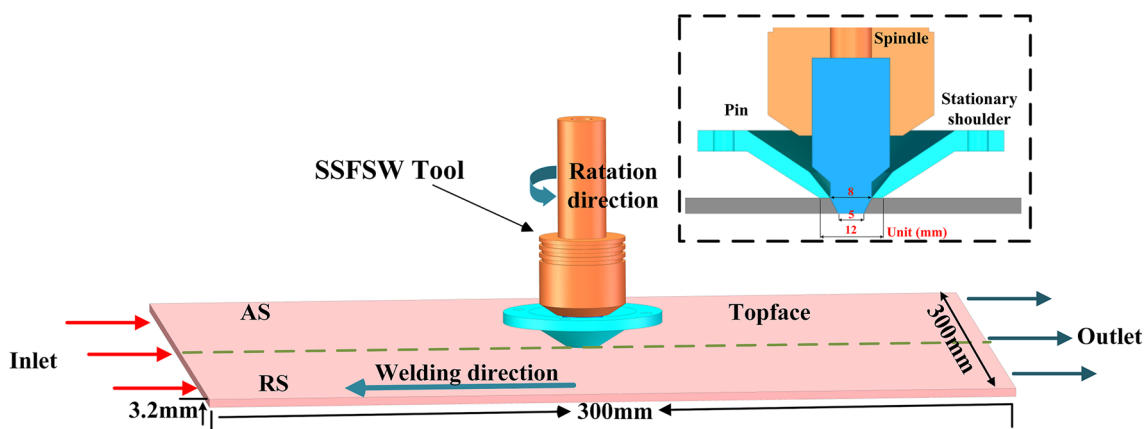
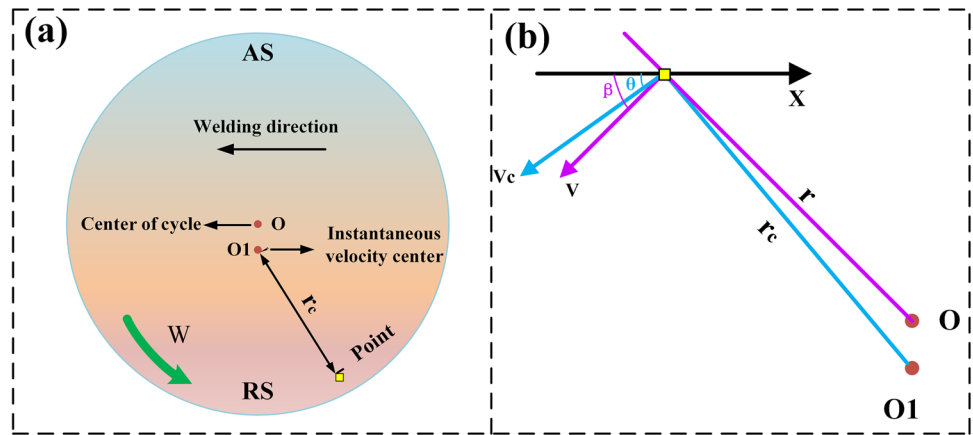


Fig. 1 Schematic of CFD model

Fig. 2 **a** Instantaneous velocity during welding. **b** Relationship between tool velocity and material velocity at the interface



$$q_{sh}(r) = \beta_2 \tau_0 U = \beta_2 [(1 - \delta)\tau_y + \delta \mu_f p_0] U \tag{6}$$

$$q_p(r) = \beta_2 \tau_0 wr = \beta_2 [(1 - \delta)\tau_y + \delta \mu_f \sigma] wr_c \cos(\beta - \theta) \tag{7}$$

$$q_b(r) = \beta_2 \tau_0 wr = \beta_2 [(1 - \delta)\tau_y + \delta \mu_f p_0] wr_c \cos(\beta - \theta) \tag{8}$$

where p_0 is the pressure applied by the shoulder and bottom of the pin; μ_f is the coefficient of friction; U is the welding speed, θ is the angle between the radius vector and welding direction, and β is the angle between the tangent direction of the circle and the welding direction. δ is the slip rate of the interface between pin and material [35], and τ_y is the yield shear strength.

$$\delta = 0.31 \times \exp\left(\frac{wr}{1.87}\right) - 0.0026 \tag{9}$$

$$\tau_y = \sigma / \sqrt{3} \tag{10}$$

3.1.2 Heat source model of boundary shear stress conditions

The heat generation exerted by friction shear stress and relative speed between pin and workpiece is given in Eqs. (11) and (12) [25, 26]:

$$q_f = \eta \times \tau_f \times \|\vec{v}\| \tag{11}$$

$$q_f = \eta \times \tau_f \times \|\vec{v}_{rel}\| \tag{12}$$

Equation (11) shows the expression of heat flux density on the shoulder during the SSFSW process and Eq. (12) shows the expression of the heat flux density at the bottom and side of pin, where τ_f is the frictional shear stress, $\|\vec{v}\|$ is the welding speed, and $\|\vec{v}_{rel}\|$ is the magnitude of relative

interface speed between tool and workpiece. η is the fraction of heat input.

3.2 Velocity near-tool-surface

3.2.1 Boundary velocity based on IVC

The plastic material flows into the calculated zone from the inlet boundary and flows out at the outlet boundary with the welding velocity in CFD simulation of the FSW process. The boundary of velocity conditions at the pin side and pin bottom is written as follows:

$$v_x = (1 - \delta)wr_c \cos(\beta - \theta) \cos\beta + wr_c \sin(\beta - \theta) \cos\left(\frac{\pi}{2} - \beta\right) \tag{13}$$

$$v_y = (1 - \delta)wr_c \cos(\beta - \theta) \sin\beta + wr_c \sin(\beta - \theta) \sin\left(\frac{\pi}{2} - \beta\right) \tag{14}$$

$$v_x = 0 \tag{15}$$

Equations (12) and (13) can correct for the angle between slip and shear stress caused by the welding speed.

3.2.2 Boundary shear stress based on IVC

$$\vec{\tau}_f = \begin{cases} \mu_f \times \sigma_n \times \frac{\vec{v}_{vel}}{\|\vec{v}_{rel}\|} \times \tanh(\alpha \times \vec{v}_{vel}), & \text{if } \vec{v}_{vel} \neq 0 \\ 0 & \text{if } \vec{v}_{vel} = 0 \end{cases} \tag{16}$$

$$\vec{v}_{vel} = (1 - \delta)\vec{v}_c \cos(\beta - \theta) \tag{17}$$

where α is scaling constant; μ_f is sliding friction coefficient; σ_n is normal force. The BSS boundary conditions employed in the present study were given by the equation below.

$$\tau_{fs} = \mu_0 \times \sigma_n \times \vec{v}_{vel} \tag{18}$$

$$\tau_{fp} = \mu_0 \times \sigma_n \times \vec{v} \tag{19}$$

$$\vec{v}_{vel} = (1 - \delta)\vec{v}_c \cos(\beta - \theta) \tag{20}$$

Equation (18) shows the boundary conditions of the shoulder during the SSFSW process and Eq. (19) shows the boundary conditions at the bottom and side of pin. The boundary conditions as well as other details about the description of this experiment and model can be found in our previous work [29, 30].

4 Results and discussion

4.1 Temperature field

Figure 3 shows the temperature distribution for different welding parameters based on the BV and BSS of the instantaneous velocity center. The heat is mainly concentrated on the pin side, and the rotation speed has a strong influence on the temperature distribution. The maximum temperature was related to the rotation speed of the stirring tool and the stirring radius, while the temperature on the advanced side(AS) was greater than on the retreating side (RS), but the position of the peak temperature did not vary with the welding parameters. The change in the position of the instantaneous velocity center indicated that, at a constant welding speed, increasing the rotation speed can reduce the distance between the instantaneous center of velocity and the center of the circle, resulting in a reduction in the difference between the radii of agitation of AS and RS, which in turn results in a smaller temperature difference between AS and RS. Compared to the modified BV, the modified BSS does not differ much in temperature distribution; their peak

temperatures are close and do not vary with the welding parameters. However, the difference in temperature between the AS and RS is greater for the welding parameter 300/15 compared to that from the BV.

Figure 4 shows the results of the temperature field calculated on different horizontal cross sections of the workpiece based on the BV and BSS. The temperature distribution during the welding process was similar under different welding conditions in Fig. 4. The high-temperature gradient at the front of the stirrer leading side (LS) and low-temperature gradient at the trailing side (TS) were influenced by the welding speed. Due to the low thermal conductivity and high density of Ti6Al4V, there is also less variation in the temperature gradient within the workpiece. As shown in Fig. 4, in the region closer to the top of the weld, the temperature of the workpiece was higher, and the thermal cycling of the temperature was greater.

In Fig. 5, the predicted and experimentally measured temperature [29] at the welding centerline along the mid-thickness plane were compared. The predicted results show good agreement with the experimental results, and the maximum difference between the predictions and the measurements is less than 5%.

4.2 Velocity field

Figure 6 shows the velocity distribution for the BSS and BV based on the IVC. The material flow was almost symmetrically distributed in the stir zone along the welding seam, and changes in rotational speed have a significant effect on the velocity values. The material flow increased significantly with increasing rotation speed, but the characteristics of the velocity distribution do not change significantly. Compared to the BV before the correction, the material velocity was reduced after the correction, but the magnitude of the change was small.

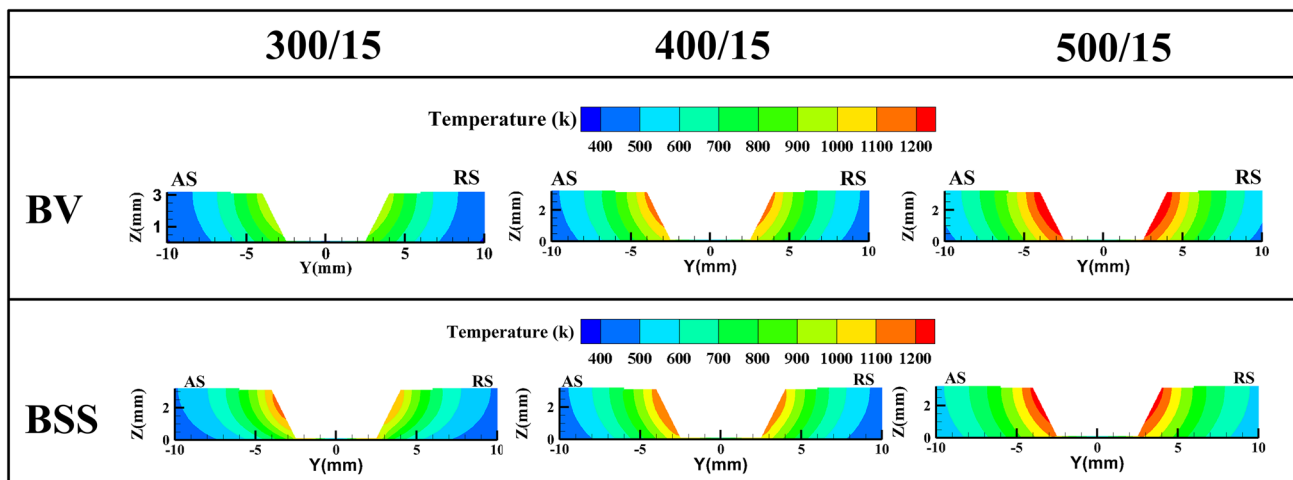


Fig. 3 Temperature distribution calculated at $x=0$ from the cross section at rotation speeds

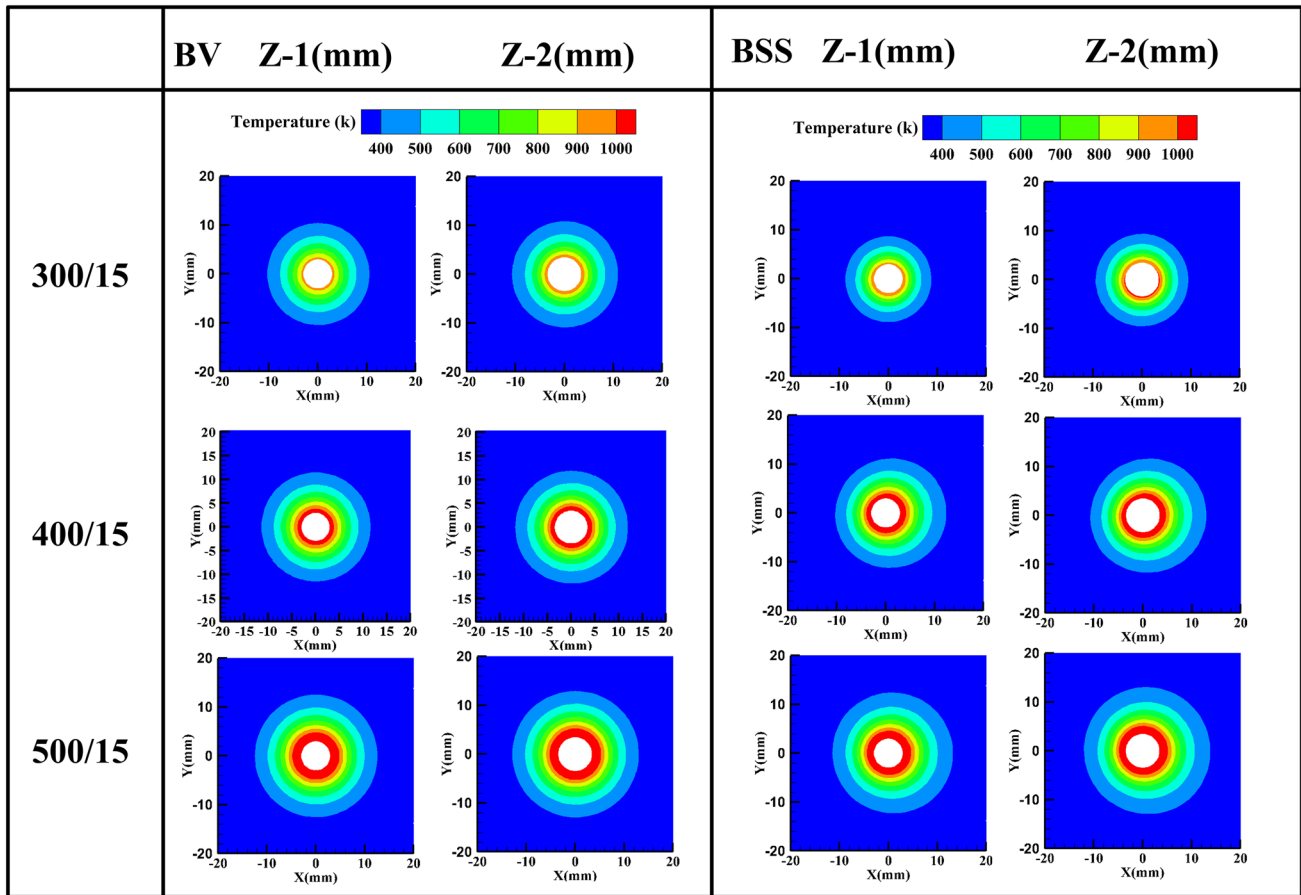


Fig. 4 Temperature distribution on the horizontal section in the middle of workpiece

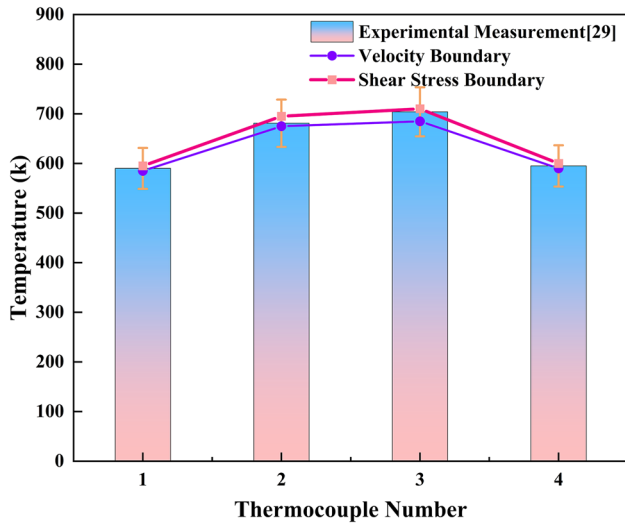


Fig. 5 Comparison of the temperature calculated by two models with measured data

This is because the slip of the welding speed was added to the model, but it was influenced by the Ti6Al4V welding parameters (the welding speed should not be too high during the welding of titanium alloys) and does not change significantly. The greatest velocities concentrated around the AS increased with increasing diameter of the stirring tool, with a corresponding increase in the velocity of the material. Therefore, the maximum value of the material velocity in the stirring area occurred at the top of pin at the AS, and the minimum velocity occurred in the region at the bottom of pin at the RS. During the welding process with heat generation of frictional and plastic deformation, the material was softened and thus adhered to the stirring tool, which in turn improves the fluidity of the weld material.

At different welding parameters, the material in the vicinity of the pin flowed around the pin. The flow area of the welded material decreased with increasing welding depth, because the influence of the pin decreased with increasing depth from the top surface, which was consistent with the cloud distribution of velocity under the BV.

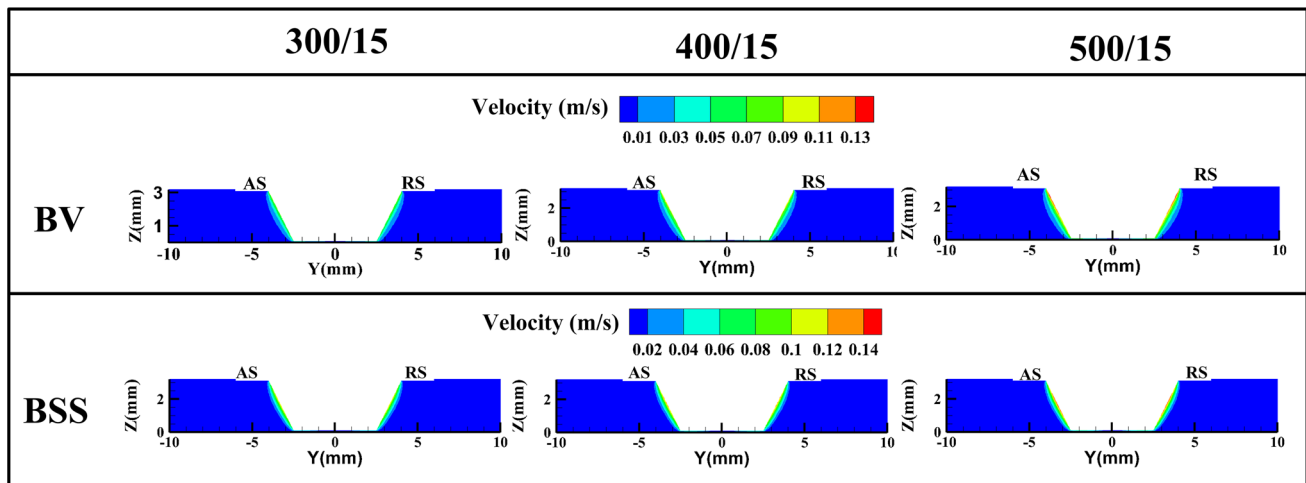


Fig. 6 Velocity distribution calculated at $x=0$ from the cross section at rotation speeds

Figures 7 shows the results of the velocity fields calculated on different horizontal cross sections of the workpiece. At the $Z=2$ mm level, the flow area of the material was larger due to the pin diameter. The velocity of the material on a horizontal plane with the same Z value increased with increasing velocity of the stirring tool, and the flow area of the material increased at different Z values of the horizontal plane; as the Z value increased, the flow area of the material increased accordingly, and the maximum material flow velocity increased accordingly.

4.3 Relationship between IVC and slip rate

To investigate the contact state of the interface based on the modified BV and BSS of IVC, the velocity distribution was extracted in the direction of the extraction path in Fig. 8. The distribution of the velocity of the material was different for the BV and for the BSS; the material velocity in the BV was similar to the velocity of the stirring tool in the extraction path with increasing stirring radius. But in the BSS, the material velocity on the bottom of the stirring tool was almost the same as the stirring tool velocity, and the velocity increased as the stirring radius increased, but it is worth noting that the maximum velocity does not occur at the maximum stirring radius. Near the junction between the bottom and pin of the stirring tool, the velocity changed abruptly and decreased sharply. The velocity then gradually increased away from the junction and decreased sharply near the top of the junction. This phenomenon was caused by interfacial slippage of the material on the side of the pin and at the junction between the side and bottom of pin.

To investigate the effect of the IVC on the slip rate, the slip rate which is in the path of Fig. 8 was extracted as shown in Fig. 9. The slip rate was distributed in two connected “W” patterns along the extraction path. The

maximum change of slip rate was at the junction between the bottom and side of pin and the junction between the side of the pin and the stationary shoulder. The change in slip rate along the extraction path was not proportional to the velocity of pin; therefore, it was found that the slip decreased along the direction of increasing velocity and increased at the junction. This is because the stirring tool junction was stationary in contact with the welded material, and the slip rate increased as it shifted from high speed to low speed. The above analysis discloses that the slip rate has a great change at the junction between the bottom and side of pin, which may be related to “relative velocity.”

4.4 Relationship between IVC and n/v

Many researchers have used the n/v ratio as an important standard of welding parameters in the past, but it is often used in empirical formulas, and few have explored the true meaning of the n/v ratio. The distance d between the instantaneous velocity center and the center of the circle is given by Eq. (21), and the result for n/v is given by Eq. (22).

$$d = v/w \tag{21}$$

where v is the welding velocity and w is the angular velocity of the stirring tool.

$$n/v = \frac{1}{2\pi} \times \frac{w}{v} = \frac{1}{2\pi} \times \frac{1}{d} \tag{22}$$

where n is the rotation speed of the stirring tool; v is the welding speed. In order to discuss more closely the effect of the instantaneous velocity center and the n/v ratio on the quality of the weld, we calculated the temperature difference

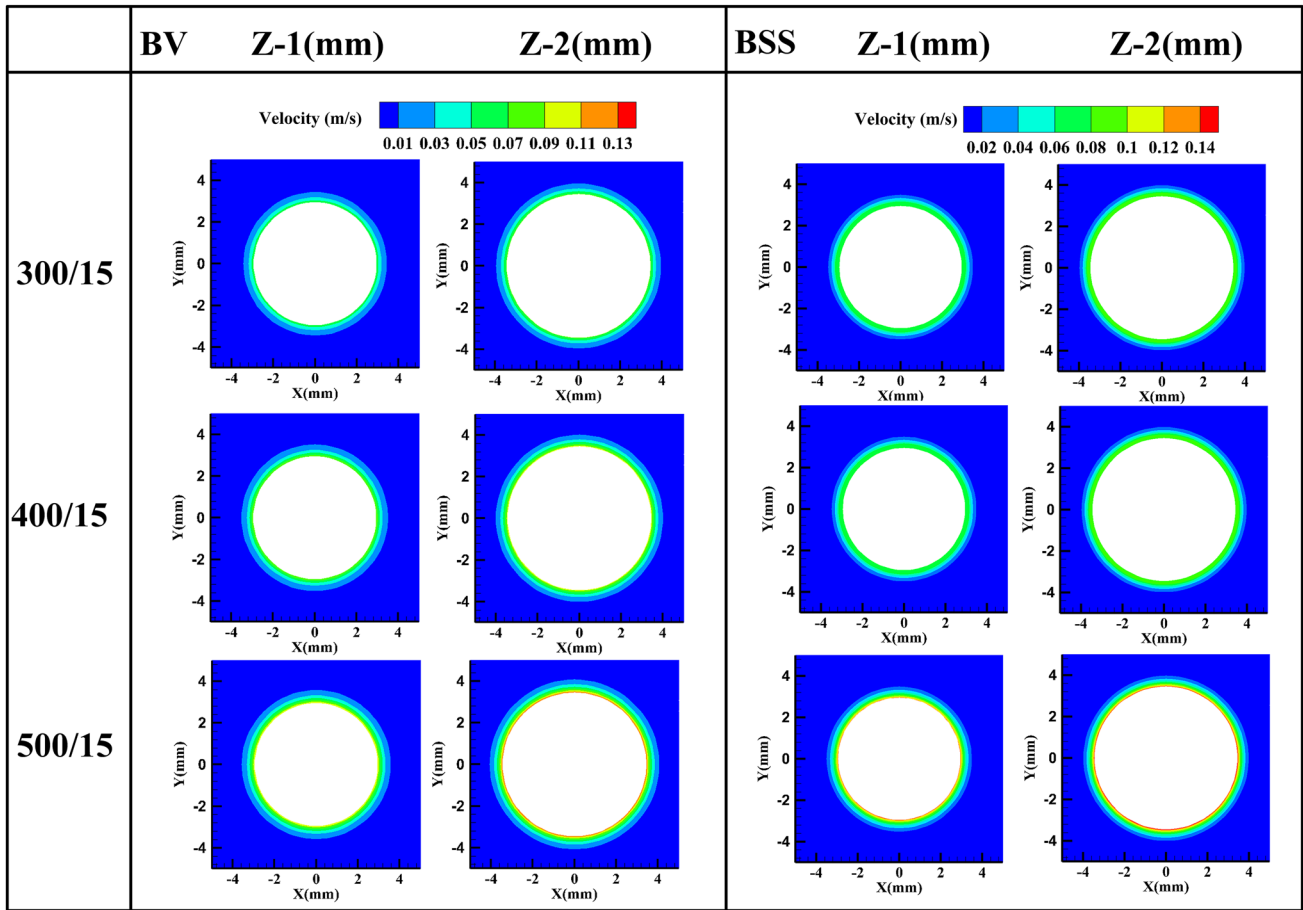


Fig. 7 Velocity distribution on the horizontal section in the middle of workpiece

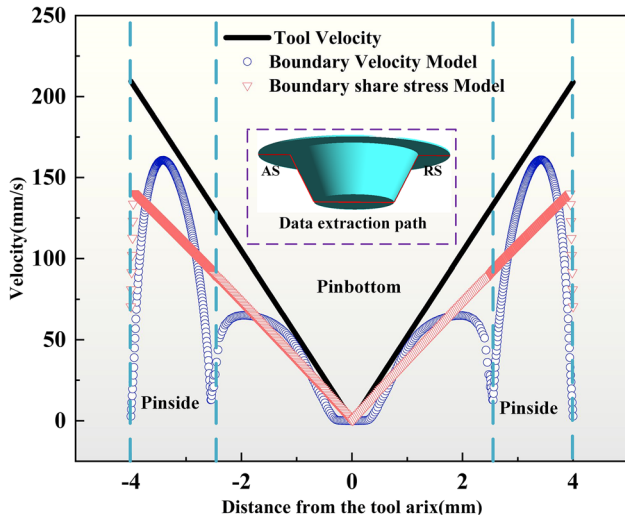


Fig. 8 The velocity of stirring tools and materials during welding based on boundary shear stress along the extraction path

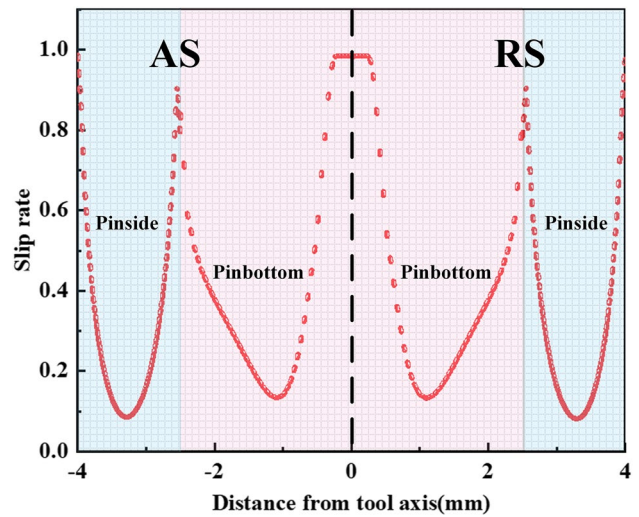


Fig. 9 Slip rate distribution along the extraction path

Table 1 The relationship between d and n/v

	500/15	400/15	300/15	500/30
d (mm)	0.00478	0.00598	0.00797	0.00956
n/v	33.33	26.67	20	16.67
Dwell time Z-1 mm (s)	24.264	24.264	24.264	12.632
Dwell time Z-2 mm (s)	28.536	28.536	28.536	14.268

between any two points in the weld material. The difference in the heat flux between AS and RS in the weld is shown in Eq. (23):

$$q_p(r) = \beta_2 \tau_0 w ((r_{c1} \cos(\beta_1 - \theta_1) - (r_{c2} \cos(\beta_2 - \theta_2))) \quad (23)$$

where β_1, θ_1 are the angle between the velocity of AS and the X direction; β_2, θ_2 are the angle between the velocity of RS and the X direction.

Table 1 shows that the distance d between the instantaneous velocity center and the center of the circle was reciprocally related to the magnitude of n/v . The instantaneous distance decreased and n/v increased with increasing speed of the stirring tool, when the difference between the heat flux on the AS and RS was reduced. In contrast, when the welding speed increased, the instantaneous center distance d increased and n/v decreased. The difference between the heat flux on the AS and the RS increased, but the heat flux decreased; the temperature of the welding process decreased. It is worth noting that the difference in temperature of thicknesses was not only dependent on the stirring radius, but also on the contact time of the stirring tool. To change the temperature difference of the thicknesses, it is necessary to change the shape of the stirring tool or to add an auxiliary heat source.

5 Conclusion

This study presents a method for calculating a new CFD model of SSFSW based on the instantaneous velocity center of the stirring tool, by modifying the BV model and the BSS model to calculate the heat production and slip rate.

- 1) A new correction model was established for the welding speed of the stirring tool in motion. The correction based on the instantaneous velocity center for the heat source model allows the slip of the welding speed to be reflected in the heat production and also corrects for errors in the projection angle of the welding speed.
- 2) The radius of rotation and the angle of rotation were modified during the welding process based on the instantaneous velocity center. The temperature distribution and the material flow were analyzed under both BV- and BSS-modified models.

- 3) This study explores the relationship between the instantaneous velocity center distance and the welding parameter n/v ratio. The instantaneous velocity center distance is inversely proportional to n/v , and its magnitude affected the temperature difference between the AS and RS.

Author contribution Wang Jiang contributed to conceptualization, methodology, validation, formal analysis, investigation, data curation, writing—original draft, writing—review and editing, visualization, supervision, and project administration. Chaojiang Li contributed to writing—original draft, writing—review and editing, supervision, project administration, and funding acquisition. Tao Yuan contributed to conceptualization, formal analysis, resources, writing—original draft, writing—review and editing, supervision, and project administration. Shujun Chen contributed to resources and writing—original draft. Hao Jing contributed to investigation and writing—original draft.

Funding This work was funded by the National Key Research and Development Program of China (No. 2022YFB3403804).

Declarations

Conflict of interest The authors declare no competing interests.

References

1. Fratini L, Buffa G (2005) CDRX modelling in friction stir welding of aluminium alloys. *Int J Mach Tools Manuf* 45:1188–1194. <https://doi.org/10.1016/j.ijmachtools.2004.12.001>
2. Bai Y, Jiang X, Chen S, Jiang W, Han Y, Yuan T, Wang X (2021) Microstructure and properties of electrically assisted stationary shoulder friction stir welded Ti6Al4V. *Sci Technol Weld Joining* 26:377–388. <https://doi.org/10.1080/13621718.2021.1923441>
3. Jiang X, Wynne BP, Martin J (2018) Variant selection in stationary shoulder friction stir welded Ti-6Al-4V alloy. *J Mater Sci Technol* 34:198–208. <https://doi.org/10.1016/j.jmst.2017.11.024>
4. He X, Gu F, Ball A (2014) A review of numerical analysis of friction stir welding. *Prog Mater Sci* 65:1–66. <https://doi.org/10.1016/j.pmatsci.2014.03.003>
5. Chen SJ, Han Y, Jiang XQ, Li XX, Yuan T, Jiang W, Wang X (2021) Study on in-situ material flow behaviour during friction stir welding via a novel material tracing technology. *J Mater Process Technol* 297:11. <https://doi.org/10.1016/j.jmatprotec.2021.117205>
6. Su Y, Li W, Liu X, Gao F, Yu Y, Vairis A (2020) Strengthening mechanism of friction stir welded alpha titanium alloy specially designed T-joints. *J Manuf Process* 55:1–12. <https://doi.org/10.1016/j.jmapro.2020.03.032>
7. Iqbal MP, Tripathi A, Jain R, Mahto RP, Pal SK, Mandal P (2020) Numerical modelling of microstructure in friction stir welding of aluminium alloys. *Int J Mech Sci* 185:105882. <https://doi.org/10.1016/j.ijmecsci.2020.105882>
8. Qian JW, Li JL, Xiong JT, Zhang FS, Li WY, Lin X (2013) Periodic variation of torque and its relations to interfacial sticking and slipping during friction stir welding. *Sci Technol Weld Joining* 17:338–341. <https://doi.org/10.1179/1362171812y.0000000001>
9. Silva YC, Oliveira Júnior FJV, Marcondes F, Silva CC (2020) Analysis of viscosity function models used in friction stir welding. *J Braz Soc Mech Sci Eng* 42. <https://doi.org/10.1007/s40430-020-02504-1>

10. Su H, Wang T, Wu C (2021) Formation of the periodic material flow behaviour in friction stir welding. *Sci Technol Weld Joining* 26:286–293. <https://doi.org/10.1080/13621718.2021.1902605>
11. Arora A, Zhang Z, De A, DebRoy T (2009) Strains and strain rates during friction stir welding. *Scripta Mater* 61:863–866. <https://doi.org/10.1016/j.scriptamat.2009.07.015>
12. Andrade DG, Leitão C, Dialami N, Chiumenti M, Rodrigues DM (2021) Analysis of contact conditions and its influence on strain rate and temperature in friction stir welding. *Int J Mech Sci* 191:106095. <https://doi.org/10.1016/j.ijmecsci.2020.106095>
13. Yu ZZ, Zhang W, Choo H, Feng ZL (2012) Transient heat and material flow modeling of friction stir processing of magnesium alloy using threaded tool. *Metall Mater Trans A-Phys Metall Mater Sci* 43A:724–737. <https://doi.org/10.1007/s11661-011-0862-1>
14. Shi L, Chen J, Yang C, Chen G, Wu C (2023) Thermal-fluid-structure coupling analysis of void defect in friction stir welding. *Int J Mech Sci* 241:107969. <https://doi.org/10.1016/j.ijmecsci.2022.107969>
15. Wu CS, Su H, Shi L (2018) Numerical simulation of heat generation, heat transfer and material flow in friction stir welding. *Acta Metall Sin* 54:265–277. <https://doi.org/10.11900/0412.1961.2017.00294>
16. Shi L, Chen J, Wu CS, Fu L (2021) Analysis of heat and mass transfer in ultrasonic vibration-enhanced friction stir welding of 2195 Al–Li alloy. *Sci Technol Weld Joining* 26:363–370. <https://doi.org/10.1080/13621718.2021.1917748>
17. Zhao W, Wu C, Su H (2020) Numerical investigation of heat generation and plastic deformation in ultrasonic assisted friction stir welding. *J Manuf Process* 56:967–980. <https://doi.org/10.1016/j.jmapro.2020.05.047>
18. Nandan R, Roy GG, Debroy T (2006) Numerical simulation of three-dimensional heat transfer and plastic flow during friction stir welding. *Metall Mater Trans A-Phys Metall Mater Sci* 37A:1247–1259. <https://doi.org/10.1007/s11661-006-1076-9>
19. Nandan R, Lienert TJ, DebRoy T (2008) Toward reliable calculations of heat and plastic flow during friction stir welding of Ti-6Al-4V alloy. *Int J Mater Res* 99:434–444. <https://doi.org/10.3139/146.101655>
20. Nandan R, DebRoy T, Bhadeshia H (2008) Recent advances in friction-stir welding - Process, weldment structure and properties. *Prog Mater Sci* 53:980–1023. <https://doi.org/10.1016/j.pmatsci.2008.05.001>
21. Liu X, Sun Z (2022) Numerical simulation of vortex- friction stir welding based on internal friction between identical materials. *Int J Heat Mass Transfer* 185:122418. <https://doi.org/10.1016/j.ijheatmasstransfer.2021.122418>
22. Huang Y, Xie Y, Meng X, Li J, Zhou L (2019) Joint formation mechanism of high depth-to-width ratio friction stir welding. *J Mater Sci Technol* 35:1261–1269. <https://doi.org/10.1016/j.jmst.2019.01.016>
23. Liechty BC, Webb BW (2008) Modeling the frictional boundary condition in friction stir welding. *Int J Mach Tools Manuf* 48:1474–1485. <https://doi.org/10.1016/j.ijmactools.2008.04.005>
24. Chen GQ, Feng ZL, Chen J, Liu L, Li H, Liu Q, Zhang S, Cao X, Zhang G, Shi QY (2017) Analytical approach for describing the collapse of surface asperities under compressive stress during rapid solid state bonding. *Scripta Mater* 128:41–44. <https://doi.org/10.1016/j.scriptamat.2016.10.015>
25. Chen G, Li H, Wang G, Guo Z, Zhang S, Dai Q, Wang X, Zhang G, Shi Q (2018) Effects of pin thread on the in-process material flow behavior during friction stir welding: a computational fluid dynamics study. *Int J Mach Tools Manuf* 124:12–21. <https://doi.org/10.1016/j.ijmactools.2017.09.002>
26. Chen G, Ma Q, Zhang S, Wu J, Zhang G, Shi Q (2018) Computational fluid dynamics simulation of friction stir welding: a comparative study on different frictional boundary conditions. *J Mater Sci Technol* 34:128–134. <https://doi.org/10.1016/j.jmst.2017.10.015>
27. Wang X, Gao Y, Liu X, McDonnell M, Feng Z (2021) Tool-workpiece stick-slip conditions and their effects on torque and heat generation rate in the friction stir welding. *Acta Materialia* 213:116969. <https://doi.org/10.1016/j.actamat.2021.116969>
28. Schmidt H, Hattel J (2005) A local model for the thermomechanical conditions in friction stir welding. *Modell Simul Mater Sci Eng* 13:77–93. <https://doi.org/10.1088/0965-0393/13/1/006>
29. Jiang W, Jiang XQ, Yuan T, Chen SJ, Liu YY, Liu XS (2022) Material flow and viscous slips during stationary shoulder friction stir welding of Ti6Al4V. *Sci Technol Weld Joining* 27:220–227. <https://doi.org/10.1080/13621718.2022.2036573>
30. Xiaoqing J, Wang J, Tao Y, Shujun C, Lei W, Yongyong L (2022) Numerical simulation of the stationary shoulder friction stir welding of Ti-6Al-4V. *J Mater Sci*. <https://doi.org/10.1007/s10853-022-07116-9>
31. Yang C, Wu C, Shi L (2020) Modeling the dissimilar material flow and mixing in friction stir welding of aluminum to magnesium alloys. *J Alloys Compd* 843:156021. <https://doi.org/10.1016/j.jallcom.2020.156021>
32. Xie Y, Meng X, Huang Y (2022) Entire-process simulation of friction stir welding — Part 2: implementation of neural networks. *Weld J* 101:172–177. <https://doi.org/10.29391/2022.101.013>
33. Xie YM, Meng XC, Huang YX (2022) Entire process simulation of friction stir welding Part I: experiments and simulation. A combined strategy for mapping the macro- and microstructural responses of aluminum alloys was proposed. *Weld J* 101:144–159. <https://doi.org/10.29391/2022.101.011>
34. Su H, Chen J, Wu C (2022) Effect of tool eccentricity on the periodic material flow in friction stir welding process. *Int J Mech Sci* 220:107164. <https://doi.org/10.1016/j.ijmecsci.2022.107164>
35. Arora A, De A, DebRoy T (2011) Toward optimum friction stir welding tool shoulder diameter. *Scripta Mater* 64:9–12. <https://doi.org/10.1016/j.scriptamat.2010.08.052>

Publisher's note Springer Nature remains neutral with regard to jurisdictional claims in published maps and institutional affiliations.

Springer Nature or its licensor (e.g. a society or other partner) holds exclusive rights to this article under a publishing agreement with the author(s) or other rightsholder(s); author self-archiving of the accepted manuscript version of this article is solely governed by the terms of such publishing agreement and applicable law.